PHOTONICS Research

Integrating InP membranes on silicon-on-insulator via tunnel epitaxy for silicon photonics

Zhao Yan,[1] Weiwei Zang,[2] Martin Ebert,[2] Bogdan-Pertin Ratiu,[1] Graham T. Reed,[2] David J. Thomson,[2] and Qiang Li[1,*]

[1]School of Physics and Astronomy, Cardiff University, Cardiff CF24 3AA, UK
[2]Optoelectronics Research Centre, University of Southampton, Southampton SO17 1BJ, UK
*Corresponding author: LiQ44@cardiff.ac.uk

Received 29 April 2025; revised 26 September 2025; accepted 27 September 2025; posted 29 September 2025 (Doc. ID 564435); published 23 December 2025

In this work, we present a tunnel epitaxy platform to integrate III–V membranes with the silicon (Si) waveguide layer on silicon-on-insulator substrates. Using metal-organic vapor-phase epitaxy, we demonstrate uniform, nearly dislocation-free InP membranes with the size of several hundred micrometers in length and a few micrometers in width. The InP membranes are positioned above Si waveguides with a thin SiN layer in between, closely resembling the vertical integration of III–V/Si bonded structures. Simulation studies reveal the versatility of the platform in fabricating hybrid modulators as well as membrane lasers with novel lateral junctions. Characterizations of the InP membranes by transmission electron microscopy and electron channeling contrast imaging show high crystalline quality. Room-temperature lasing from an InP Fabry–Pérot laser further confirms the excellent optical quality. This platform therefore offers a promising, fully epitaxial solution for next-generation Si photonics technologies.

https://doi.org/10.1364/PRJ.564435

1. INTRODUCTION

Heterogeneous Si photonics has been developed for board-to-board optical links in modern data centers. This approach typically integrates III–V wafers or dies onto Si waveguides via bonding or transfer printing [1,2]. The vertically aligned III–V devices coupled with underlying Si waveguides support efficient evanescent light coupling and modulation [3]. Leveraging the wafer bonding technique, InP membrane photonics have demonstrated high-performance lateral p-i-n devices [4–7]. The tightly confined optical modes and reduced device capacitance make this approach well-suited for high-speed, low-power applications. Membrane lasers with direct modulation rates up to 108 GHz and membrane photonic crystal lasers with ultralow power consumption of 4.4 fJ/bit have been reported [8,9].

Beyond board-to-board data communication, Si photonics is well poised to enable optical links for short-reach and ultra-short-reach interconnects, especially driven by the growing computational and data throughput demands of artificial intelligence and machine learning applications [10,11]. For large-volume, cost sensitive Si photonics applications, a Si-based manufacturing platform with integrated III–V functionalities is highly desirable [12–14]. While bonding-based technology involves sequential assembly processes, direct epitaxy on large-diameter Si or silicon-on-insulator (SOI) wafers improves scalability and reduces costs. Furthermore, selective area epitaxy can be used to produce compact III–V devices in defined areas on Si, a key advantage for short-reach optical interconnects requiring high integration density [13,14].

Over the years, three main epitaxial approaches have been developed: planar epitaxy, selective nano-ridge epitaxy, and lateral epitaxy [15]. Planar epitaxy of InAs/GaAs quantum dot lasers in conjunction with buffer engineering techniques has achieved greatly enhanced laser performance and lifetime [16]. However, the thick III–V buffer layers required may impede integration with other passive devices and hamper light coupling between III–V and Si [17,18]. Selective nano-ridge epitaxy, such as aspect ratio trapping (ART), confines epitaxy in narrow trenches on V-groove Si substrates [19,20]. Recent advances have led to GaAs-based laser diodes on 300-mm Si wafers using CMOS manufacturing lines [13]. However, the nano-ridge laser fabrication is not trivial requiring unconventional metal contact fabrication to mitigate metal-induced optical losses. More recently, the lateral epitaxy of InP on SOI has shown rapid progress, achieving butt-joint coupling with Si waveguides and enabling *in-situ* doping for lateral p-i-n

heterostructures [21–24]. High-performance photodetectors integrated with Si waveguides have been demonstrated by this approach [25,26]. However, realizing electrically driven lasers via lateral epitaxy requires further research efforts. One critical challenge is to achieve large-area, uniform epitaxial III–V membranes. This can be challenging with pits and irregularities seen at the growth fronts, often caused by rotational crystal domains and grain boundaries that compromise structural integrity [27,28].

In commercial heterogeneous bonding approaches, the III–V layer is grown separately on native substrates and then bonded onto Si waveguides in a vertical configuration [29]. If III–V-on-Si epitaxy could deliver similar vertically integrated III–V layers, existing heterogeneous Si photonics "know-how" would be accessed readily. However, no epitaxial method has yet succeeded in realizing such high-quality, vertically stacked III–V on Si waveguides with defect-free interfaces. In this work, we address these challenges by developing a tunnel epitaxy platform that enables large-area, uniform InP membranes epitaxially grown on top of the Si waveguide layer on SOI substrates. By introducing V-groove epitaxy at the beginning stage of tunnel epitaxy, we obtain InP membranes extending several hundred micrometers with minimal pits and irregularities at the growth front. Transmission electron microscopy (TEM) and electron channeling contrast imaging (ECCI) confirm that these membranes are nearly dislocation-free and free from grain boundaries. To demonstrate their optical quality, we show room-temperature optical pumped lasing from the InP Fabry–Pérot (FP) membrane lasers. We further validate the potential application of this platform through simulations of InP/Si hybrid modulators and Si waveguide coupled membrane lasers. As such, the proposed tunnel epitaxy platform shows a promising path for transitioning current heterogeneous bonding technologies to III–V/Si photonics by epitaxy.

2. DESIGN AND FABRICATION

Figure 1 illustrates the tunnel epitaxy platform. Figure 1(a) shows a schematic of InP membranes grown on SOI substrates, while Fig. 1(b) displays a tilted-view scanning electron microscopy (SEM) image of the fabricated tunnel pattern prior to epitaxy. Growth initiates from a Si V-groove within a SiN-masked cavity. As the growth transitions from vertical to lateral direction, the membranes extend over the Si waveguide layer. This initial V-groove epitaxy is crucial for forming uniform III–V seed layers and preventing grain boundaries in the lateral membranes. The epitaxially grown membranes lie above the Si waveguides, separated by a thin 20 nm SiN layer—resembling bonded InP membranes and enabling strong evanescent coupling. The lithographically defined Si waveguide can be centered beneath the tunnel for evanescent coupling. Alternatively, placing the Si waveguide at the tunnel's edge allows for III–V/Si hybrid metal-oxide-semiconductor (MOS) modulator implementations. As indicated in Fig. 1(a), we define the membrane length along the V-groove trench, while the width is along the in-plane growth direction.

Next, we use finite-difference time-domain (FDTD) simulations to assess the feasibility of device functionalities via tunnel epitaxy. Figure 1(c) shows a design for a III–V/Si hybrid modulator, where an epitaxial n-type InP membrane and a

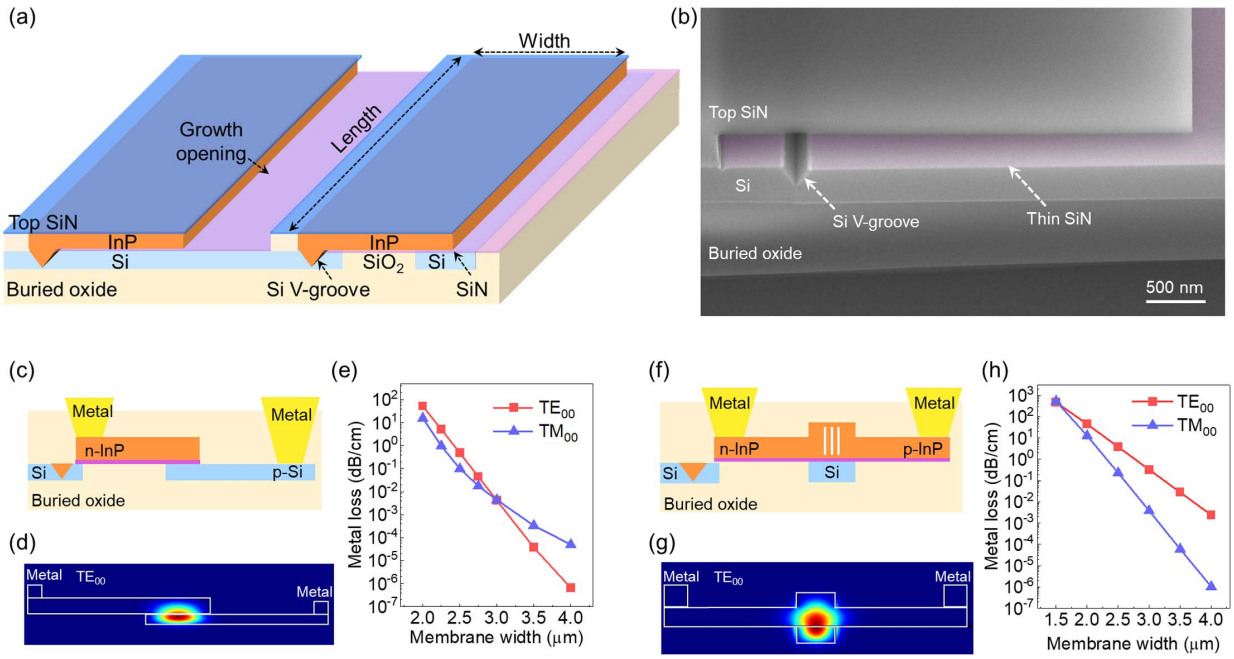

Fig. 1. (a) Schematic diagram illustrating the tunnel epitaxy for growing InP membranes on Si waveguides, initiated from a Si V-groove. The length and width directions of the InP membrane are marked for reference. (b) False-color SEM image showing the fabricated tunnel pattern prior to epitaxy. (c) Schematic representation of an electro-optic modulator (EOM) implemented using InP membranes grown via tunnel epitaxy. (d) Simulated mode profile of the fundamental TE mode. (e) Calculated metal-induced optical loss as a function of the membrane width for the EOM design. (f) Schematic illustrating a Si-waveguide-coupled, electrically driven membrane laser. (g) Simulated mode profile of the fundamental TE mode for the membrane laser. (h) Calculated metal-induced optical loss as a function of total membrane width for the membrane laser.

pre-doped p-type Si waveguide are separated by a 20-nm SiN gate dielectric layer. The thicknesses of the InP membrane and the Si waveguide are designed to be 350 nm and 220 nm, respectively, with no etched ridge structures in either layer. As shown in Fig. 1(d), the fundamental TE mode partially overlaps with the InP membrane, akin to hybrid III–V/Si MOS modulators by bonding [30,31]. Figure 1(e) explores the impact of electrode fabrication on the InP membrane. It is important to achieve sufficient width of the membrane to reduce optical loss, ensure good current injection, and to allow the direct integration of diverse waveguide structures or gratings on the III–V layer. Figure 1(f) illustrates a design of Si waveguide coupled InP membrane lasers. A 500-nm-wide ridge is etched into the InP membrane to confine the guided mode, as shown by the TE_{00} mode profile in Fig. 1(g). Figure 1(h) indicates the mode loss decreases as the membrane width increases. During in-plane InP membrane growth, vertical (110) InGaAs quantum wells (QWs) can be embedded within the membrane [white lines in the schematic of Fig. 1(f)] [32]. In conventional planar (001) QW lasers, compressive strain enhances TE gain, whereas tensile strain increases TM gain [33]. For membrane lasers with vertical (110) QWs, the trend may be reversed: compressive (110) QWs promote carrier recombination along the compressed direction (within the vertical QW plane) and could favor the TM mode, while tensile (110) QWs could amplify the TE mode. If TM lasing occurs, a Si-based passive polarization rotator may be employed to convert TM to TE mode [34]. Alternatively, the lateral InP membranes can be used as a template for the regrowth of planar (001) QWs to form a conventional vertical p-i-n junction [5]. For light detection, one could replace the Si waveguide under the tunnel with a tapered waveguide or grating coupler, similar to approaches used for Ge photodetectors in Si photonics [35,36]. These results collectively underscore the tunnel epitaxy platform's potential for integration with existing Si photonic processes.

We develop a process flow on 8-inch SOI wafers to implement the tunnel epitaxy platform. Figure 2 outlines the fabrication steps. First, an SOI wafer with pre-formed Si waveguides (Steps 1 and 2) is used, which is commonly adopted in heterogeneous integration for bonding III–V dies. We then define the tunnel patterns. In Step 3, we etch SiO_2 trenches in the top cladding and pattern a 20-nm-thick gate SiN layer. In Steps 4 and 5, a layer of amorphous Si (a-Si) is deposited and planarized via chemical mechanical polishing (CMP), with the gate SiN serving as a CMP-stop. In Step 6, another SiN layer is deposited and patterned with growth openings. Finally, in Step 7, tetramethyl ammonium hydroxide (TMAH) wet etching removes the sacrificial a-Si layer and etches the Si V-grooves, producing well-defined tunnels for epitaxy in Step 8.

3. RESULTS AND DISCUSSION

Tunnel epitaxy of InP membranes was conducted in an Aixtron close-coupled showerhead metal-organic vapor-phase epitaxy (MOVPE) system, using trimethylindium (TMIn) and tertiarybutylphosphine (TBP) as the group III and group V precursors, respectively. Before growth, a diluted hydrofluoric (HF) acid dip was performed to remove the native oxide on the Si V-groove surface. After loading into the MOVPE reactor, an *in-situ* de-oxidation was carried out at ~810°C for ~15 min. We first optimized the growth conditions to form a uniform InP seed layer in the V-groove. The growth sequence included a tertiarybutylarsine (TBA) preflow to create an arsenic-terminated Si surface, followed by depositing a low-temperature InP nucleation layer at 400°C, and then a high-temperature InP layer to finalize a uniform InP seed layer. The growth temperature was then maintained at 620°C for the lateral expansion of the InP membranes.

Figures 3(a)–3(c) show InP membranes positioned above the Si device layer, where the Si beneath the tunnel region remains unpatterned [see the tilted-view SEM image in Fig. 3(e)]. In contrast, Fig. 3(d) shows InP membranes located on top of SiO_2 (corresponding to Step 8 in Fig. 2); in the optical microscope image, these SiO_2 regions appear as gray rectangular boxes beneath the InP. For long cavity trenches, narrow SiN bridges were intentionally retained across the growth opening [Figs. 3(b)–3(d)] to provide mechanical support. The spacing between these SiN bridges ranges from 10 to 30 μm. Although we have fabricated tunnel epitaxy patterns with widths up to 7 μm, uniform membranes were only achieved with maximum widths of 3 μm in cavities as wide as 5 μm. This limitation

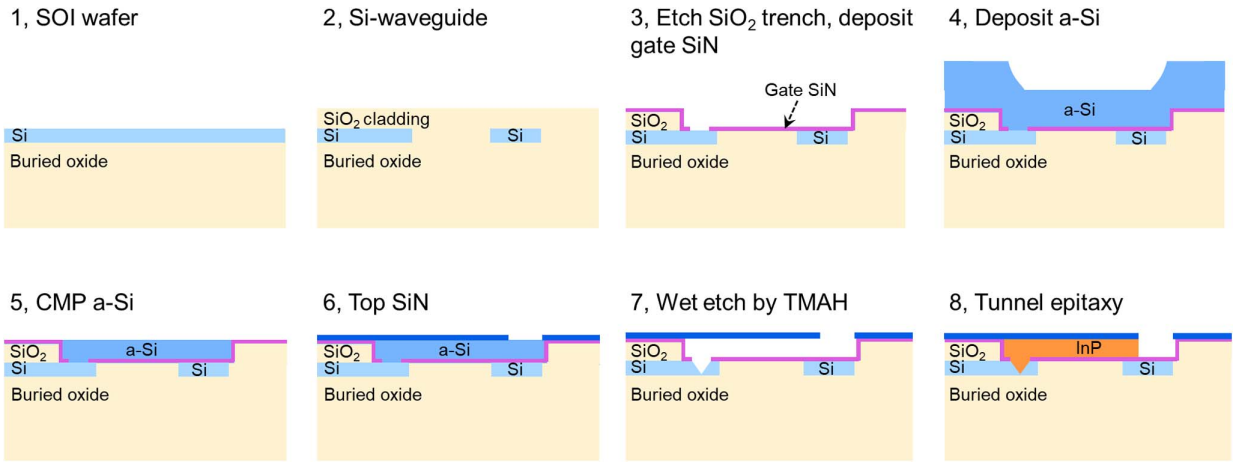

Fig. 2. Process flow for integrating InP membranes on SOI waveguide substrates using tunnel epitaxy.

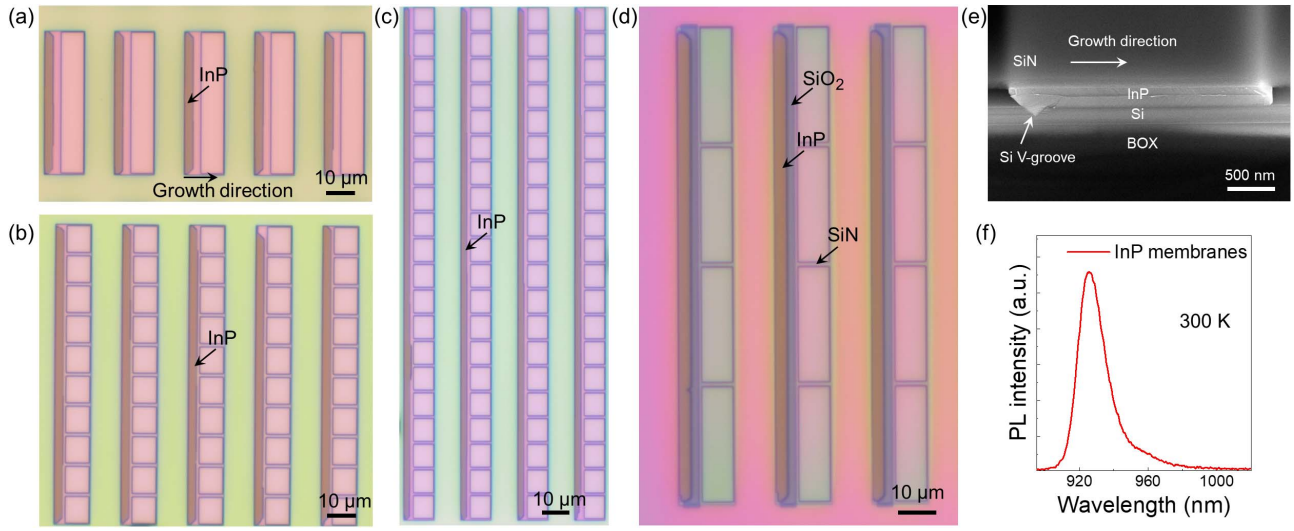

Fig. 3. Optical microscope images of epitaxial InP membranes (a)–(c) on the Si device layer and (d) on the SiO_2 layer. In (d), the SiO_2 underneath InP is identifiable as a gray rectangular block at the tunnel region. SiN bridges are also indicated in (d). (e) Cross-sectional SEM image showing InP growth within the tunnel, originating from a Si V-groove at the lower left corner. (f) μ-PL spectrum of the epitaxial InP membranes.

arises from suboptimal growth selectivity and the slow growth rate within deep trenches. Additionally, inspection over large sample areas revealed parasitic growth of sizable InP clusters. Enhancing Si patterning and improving surface cleanliness may help increase growth selectivity and enable the growth of wider membranes.

The uniform InP seeding within the Si V-groove is crucial to minimize the occurrence of pits and irregularities over extended lengths, as shown in Figs. 3(a)–3(d). Stacking faults (SFs) oriented parallel to the lateral growth direction can produce surface steps at the InP growth front. In addition, pits with an estimated density of ∼1 per 465 μm were observed over a length of 1860 μm. These pits are likely caused by imperfections in the Si fabrication process or by incomplete seeding of the III–V material in the Si V-groove. Figure 3(f) presents the micro-photoluminescence (μ-PL) spectrum of the membranes, with a peak at 930 nm, confirming the zincblende phase of InP.

We examined the crystal quality and structural integrity of the InP membranes using TEM and ECCI. Figure 4(a) shows a cross-sectional TEM image of the membrane near the V-groove side. During V-groove epitaxy, threading dislocations (TDs) and SFs appear, but remain confined to the left side of the membrane within a ∼200-nm-wide region. Notably, no additional defects arise during the vertical-to-lateral growth transition. Figure 4(b) shows a TEM image from the far end of the InP membrane, revealing that high crystal quality is maintained throughout the membranes' lateral expansion. The initial growth stage in the vertical V-grooves plays a crucial role in achieving highly uniform membranes and preventing antiphase domains (APDs). Figures 4(c) and 4(d) compare the crystal configurations for membrane growth using lateral and vertical Si V-grooves. Both types of Si V-grooves can be defined by anisotropic TMAH wet etching of Si, creating two {111} Si facets. In the lateral V-groove [Fig. 4(c)], the outmost Si layers of the upper and lower {111} Si facets are from two separate sets of the Si face-centered cubic (FCC) lattices. This results in the coexistence of Phase 1 and Phase 2 in the III–V lateral epitaxy, forming an anti-phase boundary (APB) as illustrated in Fig. 4(c). In contrast, the two {111} Si surfaces of the vertical V-groove [Fig. 4(d)] originate from the same Si FCC lattice, even in the presence of surface steps, as indicated by the red arrow in Fig. 4(d). The vertical Si V-groove surface thus effectively prevents the formation of APD or APB. Figure 4(e) shows a global-view TEM image of the InP membrane. In this sample, InGaAs quantum wells (QWs) were incorporated during growth, as seen in the central region of Fig. 4(e). A mixture of (111)A, (110), and (111)B facets was observed, along with facet evolution as additional QWs were introduced. A more detailed study of QW growth within the membranes will be presented elsewhere. We further characterized the InP membranes using ECCI, which corroborated TEM findings. Figures 4(f) and 4(g) show paired top-view SEM and ECCI images taken after the removal of the top SiN layer, where no APBs are observed. We observed SFs similar to those found in III–V nano-ridges parallel to the trench [37]. These SFs generally traverse the membrane without introducing partial dislocations.

To evaluate the optical quality of the membranes, we removed the underlying SiO_2 and Si layers with HF and potassium hydroxide (KOH) wet etch and transferred the InP membranes onto a SiO_2/Si substrate, as shown in Fig. 5(a). The cross-sectional SEM image in Fig. 5(b) shows the suspended membrane after SiO_2 and Si removal. Figure 5(c) displays the membrane on a SiO_2/Si substrate, with two FP end facets formed by breaking a long membrane. The inset in Fig. 5(c) provides a close-up SEM image, highlighting the V-groove region.

We tested the fabricated InP membrane laser using a home-built μ-PL system. The pump source was a pulsed laser at 780 nm wavelength, with an 80 MHz repetition rate and a 100 fs pulse width. A semicylindrical prism was used to shape the incident beam into a line with an area of approximately

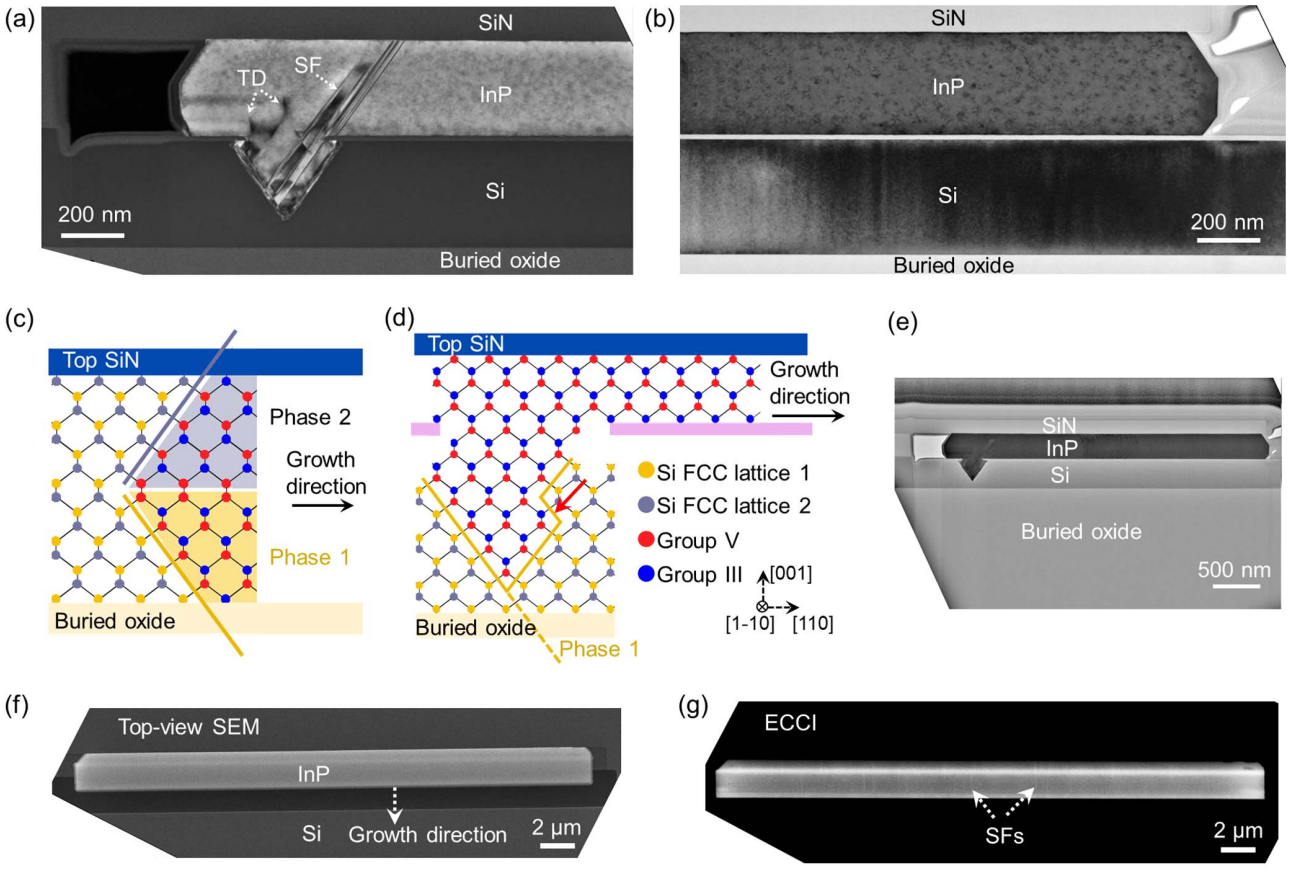

Fig. 4. (a) Cross-sectional TEM image of the InP membrane near the vertical V-groove region. (b) TEM image at the end of the InP membrane. (c) Crystal configuration illustrating III–V epitaxy from a lateral Si V-groove, resulting in the formation of both phases. (d) Crystal configuration illustrating III–V epitaxy from a vertical Si V-groove with surface steps. (e) Global-view TEM image of the InP membrane. (f), (g) Top-view SEM and ECCI images of the InP membrane after removal of the top SiN layer.

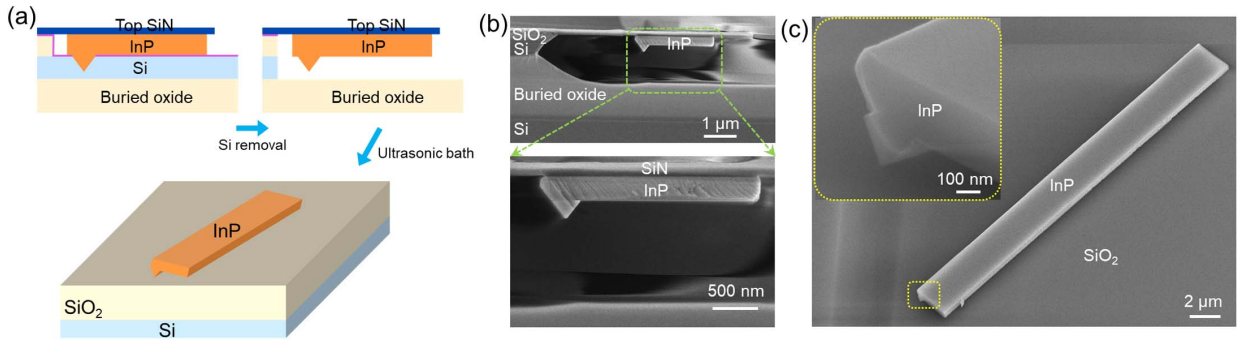

Fig. 5. (a) Process flow for fabricating the InP FP membrane laser. (b) Cross-sectional SEM image of the suspended InP membrane after SiO_2 and Si removal. (c) SEM image of the fabricated InP membrane laser; the inset highlights the underlying InP V-groove seed and the overlying membrane.

35 μm × 2.5 μm, covering the entire InP membrane laser area. Emitted light was detected using a two-dimensional InGaAs focal plane array (FPA) cooled to −80°C. Figure 6 shows the evolution of the membrane laser's emission spectra with increasing pump power. As pump power rises, the emission transitions from spontaneous emission to discrete modes and finally to dominant lasing. As shown in Fig. 6(b), spontaneous emission is strongly suppressed once lasing begins. The light–light (L–L) curve and linewidth narrowing in Fig. 6(c) confirm lasing with a threshold at ~80 μJ/cm^2. Figure 6(d) shows emission images captured by the FPA at various pump powers. Because of the membrane laser's length and the spectrometer's slit width limit, a single image cannot capture the entire FP laser emission. Consequently, the image at 83.4 μJ/cm^2 is stitched from multiple frames. These images demonstrate that the membrane laser effectively functions as an FP cavity,

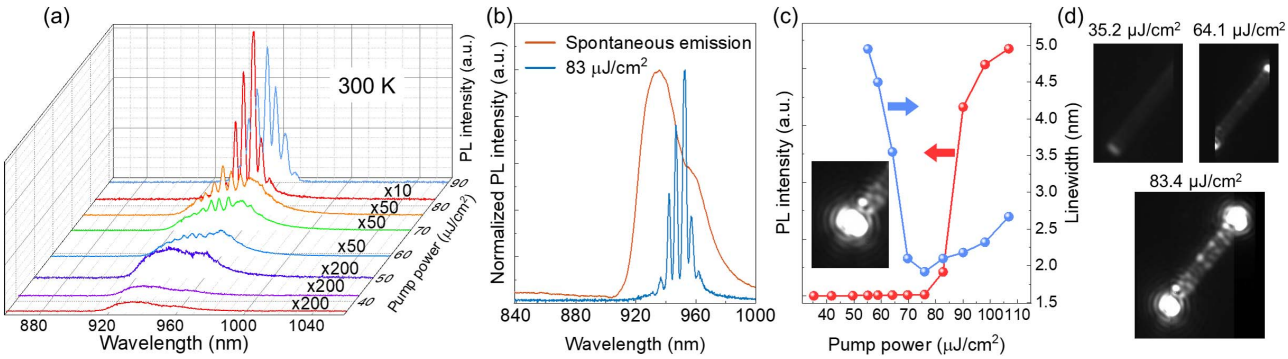

Fig. 6. (a) Room-temperature spectral evolution of the membrane laser with increasing pump power. (b) The collected lasing spectrum (blue) above threshold of an FP membrane laser and the spontaneous emission spectrum (orange) below threshold. (c) Light–light (L–L) curve and linewidth narrowing of the lasing peak at various pump powers; the inset shows the lasing fringe pattern at one end of the FP cavity. (d) Emission images from the membrane laser at different pump powers. The image at 83.4 $\mu J/cm^2$ is a stitched montage due to the laser's length exceeding the spectrometer's slit width.

emitting from both ends. Above the lasing threshold, a clear fringe pattern emerges, as seen in Fig. 6(d).

Finally, InP membranes grown via tunnel epitaxy maintain a planar structure with a thickness comparable to standard Si photonic waveguides. This structural compatibility ensures that the mode size and shape in the III–V membrane closely match those in the Si waveguides, enabling efficient optical coupling. This contrasts with previous epitaxy approaches, such as planar epitaxy of III–V lasers with thick cladding layers and less-confined modes, which required long III–V tapers for coupling and led to increased free carrier absorption loss, or selective area epitaxy of III–V nano-ridges with non-planar structures that may not align with the fundamental TE mode in the planar Si waveguide.

4. CONCLUSION

We have developed a tunnel epitaxy platform for integrating InP membranes with silicon-on-insulator substrate technology. The approach of tunnel epitaxy achieves not only membrane structures of excellent crystalline quality, but also seamless integration of InP membranes with Si waveguides. In contrast to many existing epitaxy approaches, the tunnel epitaxy platform demonstrates high versatility and strong compatibility with present Si photonics platforms. It therefore shows a promising path to enable the transitioning of current heterogeneous integration technologies to future monolithic integrated III–V/Si photonics by epitaxy.

Funding. Engineering and Physical Sciences Research Council (EP/T01105X/1, EP/Z536167/1); Future Compound Semiconductor Manufacturing Hub (EP/P006973/1); Rockley Photonics prosperity partnership (EP/R003076/1); Royal Society (UF150325).

Disclosures. The authors declare no conflicts of interest.

Data Availability. Data supporting the findings of this study are available in Ref. [38].

REFERENCES

1. T. Komljenovic, M. Davenport, J. Hulme, *et al.*, "Heterogeneous silicon photonic integrated circuits," J. Lightwave Technol. **34**, 20–35 (2016).
2. J. Zhang, G. Muliuk, J. Juvert, *et al.*, "III-V-on-Si photonic integrated circuits realized using micro-transfer-printing," APL Photonics **4**, 110803 (2019).
3. B. Szelag, K. Hassan, L. Adelmini, *et al.*, "Hybrid III–V/silicon technology for laser integration on a 200-mm fully CMOS-compatible silicon photonics platform," IEEE J. Sel. Top. Quantum Electron. **25**, 8201210 (2019).
4. K. Hasebe, T. Sato, K. Takeda, *et al.*, "High-speed modulation of lateral p-i-n diode structure electro-absorption modulator integrated with DFB laser," J. Lightwave Technol. **33**, 1235–1240 (2015).
5. T. Fujii, K. Takeda, H. Nishi, *et al.*, "Multiwavelength membrane laser array using selective area growth on directly bonded InP on SiO_2/Si," Optica **7**, 838–846 (2020).
6. N. Diamantopoulos, T. Fujii, S. Yamaoka, *et al.*, "16-channel directly modulated membrane III-V laser array on SiO_2/Si utilizing photon-photon resonance," J. Lightwave Technol. **42**, 3997–4005 (2024).
7. Y. Jiao, N. Nishiyama, J. van der Tol, *et al.*, "InP membrane integrated photonics research," Semicond. Sci. Technol. **36**, 013001 (2021).
8. K. Takeda, T. Sato, A. Shinya, *et al.*, "Few-fJ/bit data transmissions using directly modulated lambda-scale embedded active region photonic-crystal lasers," Nat. Photonics **7**, 569–575 (2013).
9. S. Yamaoka, N. Diamantopoulos, H. Nishi, *et al.*, "Directly modulated membrane lasers with 108 GHz bandwidth on a high-thermal-conductivity silicon carbide substrate," Nat. Photonics **15**, 28–35 (2021).
10. N. Margalit, C. Xiang, S. M. Bowers, *et al.*, "Perspective on the future of silicon photonics and electronics," Appl. Phys. Lett. **118**, 220501 (2021).
11. M. Khani, M. Ghobadi, M. Alizadeh, *et al.*, "SiP-ML: high-bandwidth optical network interconnects for machine learning training," in *SIGCOMM'21: Proceedings of the 2021 ACM SIGCOMM 2021 Conference* (2021), pp. 657–675.
12. A. Y. Liu and J. Bowers, "Photonic integration with epitaxial III–V on silicon," IEEE J. Sel. Top. Quantum Electron. **24**, 6000412 (2018).
13. Y. Koninck, C. Caer, D. Yudistira, *et al.*, "GaAs nano-ridge laser diodes fully fabricated in a 300-mm CMOS pilot line," Nature **637**, 63–69 (2025).
14. Y. Han, H. Park, J. Bowers, *et al.*, "Recent advances in light sources on silicon," Adv. Opt. Photonics **14**, 404–454 (2022).
15. Z. Yan and Q. Li, "Recent progress in epitaxial growth of dislocation tolerant and dislocation free III–V lasers on silicon," J. Phys. D Appl. Phys. **57**, 213001 (2024).
16. C. Shang, E. Hughes, Y. Wan, *et al.*, "High-temperature reliable quantum-dot lasers on Si with misfit and threading dislocation filters," Optica **8**, 749–754 (2021).

17. W. Wei, A. He, B. Yang, *et al.*, "Monolithic integration of embedded III-V lasers on SOI," Light Sci. Appl. **12**, 84 (2023).
18. C. Shang, K. Feng, E. T. Hughes, *et al.*, "Electrically pumped quantum-dot lasers grown on 300 mm patterned Si photonic wafers," Light Sci. Appl. **11**, 299 (2022).
19. B. Kunert, Y. Mols, M. Baryshniskova, *et al.*, "How to control defect formation in monolithic III/V hetero-epitaxy on (100) Si? A critical review on current approaches," Semicond. Sci. Technol. **33**, 093002 (2018).
20. Y. Han, Y. Xue, Z. Yan, *et al.*, "Selectively grown III-V lasers for integrated Si-photonics," J. Lightwave Technol. **39**, 940–948 (2021).
21. Z. Yan, Y. Han, L. Lin, *et al.*, "A monolithic InP/SOI platform for integrated photonics," Light Sci. Appl. **10**, 200 (2021).
22. Y. Han, Z. Yan, Y. Xue, *et al.*, "Micrometer-scale InP selectively grown on SOI for fully integrated Si-photonics," Appl. Phys. Lett. **117**, 052102 (2020).
23. Y. Xue, Y. Han, Y. Tong, *et al.*, "High-performance III-V photodetectors on a monolithic InP/SOI platform," Optica **8**, 1204–1209 (2021).
24. D. Fu, Z. Ren, Y. Jin, *et al.*, "Buried InGaAs/InP quantum wells selectively grown on SOI for lateral membrane laser diodes," Appl. Phys. Lett. **124**, 081102 (2024).
25. P. Wen, P. Tiwari, S. Mauthe, *et al.*, "Waveguide coupled III-V photodiodes monolithically integrated on Si," Nat. Commun. **13**, 909 (2022).
26. Y. Xue, Y. Han, Y. Wang, *et al.*, "High-speed and low dark current silicon-waveguide-coupled III-V photodetectors selectively grown on SOI," Optica **9**, 1219–1226 (2022).
27. H. Homma, H. Sugiyama, T. Hiraki, *et al.*, "Microstructural characterization of InP films on SOI (001) substrates grown by selective lateral metal-organic vapor-phase epitaxy," J. Cryst. Growth **648**, 127903 (2024).
28. Z. Yan, B. Ratiu, W. Zhang, *et al.*, "Lateral tunnel epitaxy of GaAs in lithographically defined cavities on 220 nm silicon-on-insulator," Cryst. Growth Des. **23**, 7821–7828 (2023).
29. C. Xiang, W. Jin, D. Huang, *et al.*, "High-performance silicon photonics using heterogeneous integration," IEEE J. Sel. Top. Quantum Electron. **28**, 8200515 (2022).
30. T. Hiraki, T. Aihara, K. Hasebe, *et al.*, "Heterogeneously integrated III–V/Si MOS capacitor Mach–Zehnder modulator," Nat. Photonics **11**, 482–485 (2017).
31. J. Han, F. Boeuf, J. Fujikata, *et al.*, "Efficient low-loss InGaAsP/Si hybrid MOS optical modulator," Nat. Photonics **11**, 486–490 (2017).
32. Z. Lei, D. Fu, Y. Han, *et al.*, "Strain engineering of vertical (110) InGaAs/InP quantum wells laterally grown on (001) SOI," Appl. Phys. Lett. **126**, 182104 (2025).
33. A. R. Adams, "Strained-layer quantum-well lasers," IEEE J. Sel. Top. Quantum Electron. **17**, 1364–1373 (2011).
34. H. Zafar and M. F. Pereira, "Recent progress in light polarization control schemes for silicon integrated photonics," Laser Photonics Rev. **18**, 2301025 (2024).
35. S. Lischke, A. Peczek, J. S. Morgan, *et al.*, "Ultra-fast germanium photodiode with 3-dB bandwidth of 265 GHz," Nat. Photonics **15**, 925–931 (2021).
36. G. Chen, Y. Yu, Y. Shi, *et al.*, "High-speed photodetectors on silicon photonics platform for optical interconnect," Laser Photonics Rev. **16**, 2200117 (2022).
37. Y. Han, Z. Yan, W. K. Ng, *et al.*, "Bufferless 1.5 μm III-V lasers grown on Si-photonics 220 nm silicon-on-insulator platforms," Optica **7**, 148–153 (2020).
38. https://doi.org/10.17035/cardiff.30203509.